Supporting information for

Highly graphitized nitrogen-doped ordered mesoporous carbon supported Ni nanocrystals for efficient hydrazine-assisted CO_2 splitting

Kang Lian[a,b], Junyang Ding[c], Jin Zhang[a], Quan Zhang[b,c]*,Yifan Liu[d], Guangzhi Hu[e], and Xijun Liu[c]**

a) *School of Public Health/Key Laboratory of Endemic and Ethnic Diseases, Ministry of Education & Key Laboratory of Medical Molecular Biology of Guizhou Province, Guizhou Medical University, Guiyang 561113, China*

b) *Institute for New Energy Materials & Low-Carbon Technologies, School of Materials Science and Engineering, Tianjin University of Technology, Tianjin 300384, China*

c) *State Key Laboratory of Featured Metal Materials and Life-cycle Safety for Composite Structures, Guangxi Key Laboratory of Processing for Non-ferrous Metals and Featured Materials, School of Resources, Environment and Materials, Guangxi University, Nanning 530004, China*

d) *Institute of Advanced Science Facilities, Shenzhen 518107, Guangdong, China*

e) *Institute for Ecological Research and Pollution Control of Plateau Lakes School of Ecology and Environmental Science, Yunnan University, Kunming 650504, China*

*Corresponding authors: jzhang@gmc.edu.cn; 18230299580@163.com; xjliu@gxu.edu.cn

1. Material synthesis

Ni-NC is readily prepared through hard-template wet synthesis and the following pyrolytic treatment. In a typical synthesis, 0.5 g of ordered mesoporous silica (SBA-15, purchased from XFNANO) and 0.22 g of nickel chloride hexahydrate ($NiCl_2 \cdot 6H_2O$, bought from Aladdin) are uniformly mixed in 3.0 mL of deionized water (prepared in the laboratory). After air-drying, the resulting Ni precursor is transferred to a 50 mL round-bottom flask containing 2.0 g of ethylenediamine (EDA, obtained from Sinopharm) and 4.0 g of carbon tetrachloride (CTC, acquired from Innochem). After thorough ultrasonic dispersion, a homogeneous pink mixture is observed in the flask, which is then stirred and refluxed at 90 °C for 6 hours until complete polymerization of EDA and CTC. The resulting brownish polymer is carbonized in a 900 °C argon-hydrogen mixed atmosphere (9: 1) with a heating rate of 5 °C min^{-1} for 2 hours. Finally, the carbonaceous compound is etched with 8 wt% hydrofluoric acid (HF, purchased from Aladdin) for 12 hours, washed repeatedly with deionized water, and dried to obtain Ni-NC. The synthesis of the Ni-NC-*X* series (*X* = 0.1, 0.5, 1.5) follows the same steps as described above, with the only variation being the amount of nickel incorporated. In the corresponding steps, $NiCl_2 \cdot 6H_2O$ is added in amounts of 0.1 (0.022 g), 0.5 (0.11 g), and 1.5 (0.33 g) times that used for Ni-NC. The synthesis of NC also follows the same steps as described above, but without the addition of $NiCl_2 \cdot 6H_2O$.

2. Material Characterization

Scanning electron microscopy (SEM) images were taken on a Nova NanoSEM450 scanning electron microscope. Transmission electron microscopy (TEM) measurements were performed on a JEM-ARM 200F transmission electron microscope. Powder X-ray diffraction

(XRD) patterns were obtained by an X-ray diffractometer (Rigaku SmartLab) at a scan rate of 10° min^{-1} with Cu Kα radiation (λ = 0.154598 nm). Raman spectrum was recorded on a Raman microscope of Horiba Evolution. N_2 adsorption-desorption isotherms were measured on an Autosorb-IQ3+ChemStar. Specific surface areas were calculated by the Brunauer-Emmett-Teller (BET) method and pore sizes were obtained by a non-local density functional theory (NLDFT) method. X-ray photoelectron spectroscopy (XPS) was collected by a Thermo Scientific ESCALAB250Xi photoelectron spectrometer equipped with the Al Kα (1486.6 eV) radiation as the X-ray source and the C 1*s* peak was fixed at the binding energy of 284.8 eV.

3. Electrochemical measurements

All electrochemical tests were performed at room temperature using a CHI760e electrochemical workstation. Linear sweep voltammetry (LSV) curves were recorded at a scan rate of 5 mV s^{-1} without infrared compensation. Current densities were calculated based on the geometric area of the working electrode and were normalized to the reversible hydrogen electrode (RHE).

3.1 CO_2RR measurements

Typical CO_2 reduction reaction (CO_2RR) was conducted using a closed H-type cell separated by a proton exchange membrane (Nafion 115). Both compartments were filled with 0.5 M $KHCO_3$ aqueous solution as the electrolyte. The Ag/AgCl electrode and Pt foil were used as reference electrode and counter electrode, respectively. The working electrode was prepared by applying ink (e.g., Ni-NC or NC) onto hydrophobic carbon paper to achieve a loading of 1 mg cm^{-2}. Prior to the experiment, the electrolyte in the cathode compartment

was saturated with CO_2/Ar. All potential for CO_2RR were converted according to the following equation:

$$E_{RHE} = E_{Ag/AgCl} + 0.0591 \times pH + 0.197 \quad \text{Eq. S1}$$

where *pH* of the CO_2-saturated 0.5 M $KHCO_3$ was determined as 7.32.

3.2 HzOR measurements

The hydrazine oxidation reaction (HzOR) and water oxidation reaction (OER) were conducted using a single-pool reactor, with electrolytes consisting of 1 M KOH with 0.5 M N_2H_4 solution and 1 M KOH solution, respectively. The Hg/HgO electrode and carbon rod were employed as reference and counter electrodes, respectively. The preparation of the working electrode was analogous to that used in CO_2RR, except that hydrophilic carbon paper was selected for its fabrication. During HzOR durability testing, the electrolyte was periodically refreshed to ensure a sufficient supply of N_2H_4. All potential of HzOR and OER were calculated according to the following equation:

$$E_{RHE} = E_{Hg/HgO} + 0.059 \times pH + 0.098 \quad \text{Eq. S2}$$

where *pH* of HzOR and OER were determined as 13.88.

3.3 HECR measurements

For the energy-efficient coupling of HzOR with CO_2RR (HzOR||CO_2RR), the process was conducted in a two-electrode sealed H-type cell equipped with a bipolar membrane. The anode and cathode were prepared similarly to the working electrodes used in HzOR and CO_2RR. Anode chamber employed an electrolyte of 1 M KOH with 0.5 M N_2H_4, while the cathode chamber used 0.5 M $KHCO_3$ solution. During durability testing, the anode electrolyte was periodically refreshed to ensure a sufficient supply of N_2H_4. For comparison,

a traditional water oxidation-coupled CO_2RR (OER||CO_2RR) anode utilized 1 M KOH solution as the electrolyte. Compared to OER||CO_2RR, the energy saving efficiency (η) for energy-efficient HzOR||CO_2RR was calculated based on the required voltages of the full cell from the following equation [1]:

$$\eta = (E_{OER||CO2RR} - E_{HzOR||CO2RR}) / E_{OER||CO2RR} \times 100\% \quad \text{Eq. S3}$$

Further evaluation of the HzOR||CO_2RR system is conducted within a membrane electrode assembly (MEA). The catalyst layer, with a loading of 1 mg cm^{-2}, is tightly deposited on both sides of the anion exchange membrane, with stable titanium felt serving as the anode, and a gas diffusion electrode, formed by hydrophobic carbon paper, functioning as the cathode. The anode chamber employs an electrolyte consisting of a 1 M KOH solution containing 0.5 M N_2H_4, whereas the cathode chamber is supplied with humidified CO_2. In contrast, the conventional OER||CO_2RR configuration utilizes a 1 M KOH solution at the anode, with the remaining setup mirroring that of the HzOR||CO_2RR.

3.4 EIS and ECSA measurements

EIS was performed at an open-circuit potential state in the frequency range from 1000 kHz to 0.1 Hz with a voltage amplitude of 5 mV. To determine the double-layer capacitance (C_{dl}) of the material within the non-Faradaic potential range, measurements were conducted at various scan rates. The electrochemical surface area (ECSA) was calculated using the following equation:

$$R_f = C_{dl} / C_S \quad \text{Eq. S4}$$

$$\text{ECSA} = R_f \times S \quad \text{Eq. S5}$$

where R_f is the roughness factor, C_S is the specific capacitance of the carbon-based support (1.03 mF cm^{-2}) [2]. S is the geometric active area (1 × 1 cm^2).

3.5 TOF measurements

TOF values were calculated according to the previously reported equation [3,4]:

$$TOF = (j \times S) / (\alpha \times F \times n) \quad \text{Eq. S6}$$

where j is the HzOR current density; S is the geometric active area (1 × 1 cm^2); α is 4 for HzOR; and F is the Faraday constant (96485 C mol^{-1}). The n values were measured by a widely used method [5]: Cyclic voltammetry (CV) measurements were performed when the scan rate was fixed at 50 mV s^{-1}. After this, by integrating the charge of CV curve over the whole potential range, the half value of the charge was obtained, which is the value of the surface charge density (Q_S). Then, the n value was calculated using the following equation:

$$n = Q_S / F \quad \text{Eq. S7}$$

where F is the Faraday constant (96485 C mol^{-1}).

4. Product analysis

Gaseous products of CO_2RR were monitored by a gas chromatograph (GC, Agilent 7890B) equipped with a flame ionization detector (FID) and thermal conductivity detector (TCD). Electrolyte solution was collected from the cathode chamber after electrolysis and characterized by Avance III HD 400MHz ^{1}H nuclear magnetic resonance (^{1}H NMR). Faraday efficiency of CO (FE_{CO}) was calculated as the following equation:

$$FE_{CO} = (2 \times m \times F)/Q = (2 \times C_{gas} \times V_{CO2} \times 10^{-3} \times t \times F)/(24.8 \times Q) \quad \text{Eq. S8}$$

where m is the mol amount of CO; F is the Faraday constant (96485 C mol^{-1}); Q is the total quantity of electric charge during the CO_2RR at a constant current density; C_{gas} is the volume concentration of the gas products, originating from the GC; V_{CO2} is the flow rate of CO_2 (30 mL min^{-1}); t is electrolysis time.

5. In situ FTIR measurements

In situ fourier transform infrared (In situ FTIR) were recorded using a Bruker FTIR spectrometer (CRCP-7070-A). A gilded silicon hemispherical prism served as both the conductive substrate and the infrared reflection element, while the Ni-NC was deposited on the Au/Si surface to function as the working electrode. For CO_2RR, Ag/AgCl and Pt wire were utilized as the reference and counter electrodes, respectively, while the electrolyte consisted of a CO_2-saturated 0.5 M $KHCO_3$ solution. For the HzOR, a Hg/HgO electrode served as the reference electrode, and a carbon rod was used as the counter electrode, with a 1 M KOH solution containing 0.5 M N_2H_4 as the electrolyte. During the progressive potential of the working electrode, spectral signals were collected at a resolution of 4 cm^{-1}, with 20 scans performed for each applied potential.

6. DFT calculations

All density functional theory (DFT) calculations were performed using the Vienna Ab initio Simulation Package (VASP). For the treatment of electronic exchange and correlation effects, the Perdew-Burke-Ernzerhof exchange-correlation functional, based on the generalized gradient approximation, was employed. The kinetic energy cutoffs for the plane-wave basis set were fixed at 500 eV to ensure accurate energy convergence. The Brillouin zone was

sampled with a 1 × 1 × 1 k-point grid across all computational models to achieve sufficient precision. A vacuum region of 20 Å was introduced along the Z-axis to minimize spurious interactions between periodic images. The convergence thresholds were rigorously set to 10^{-5} eV for electronic self-consistency and 0.05 eV $Å^{-1}$ for ionic relaxation. The free energy change (ΔG) of each adsorbed intermediate was computed using the following expression:

$$\Delta G = \Delta E + \Delta ZPE - T\Delta S \quad \text{Eq. S9}$$

Where ΔE, ΔZPE and ΔS represent the changes in electronic energy, zero-point energy, and entropy associated with the adsorption of intermediates, respectively. The thermodynamic corrections at the reaction temperature (298 K) were calculated using the VASPKIT software suite.

Figures and Tables

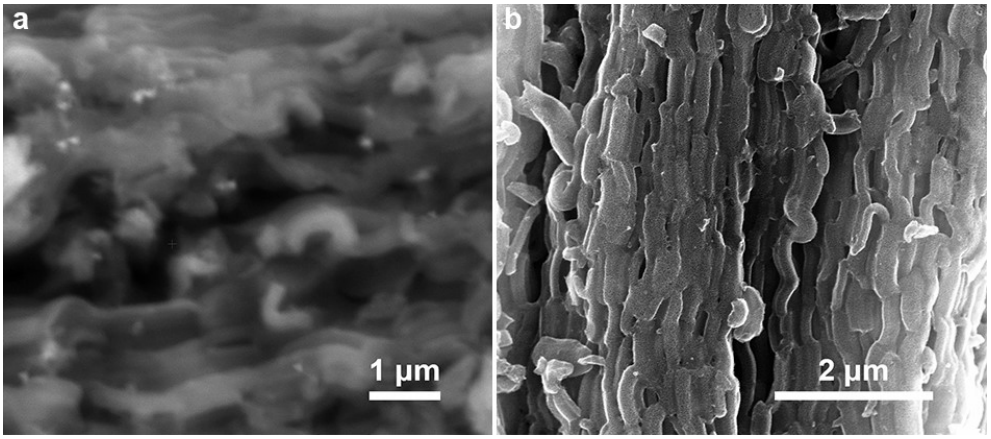

Fig. S1. SEM images of a) Ni-NC and b) NC.

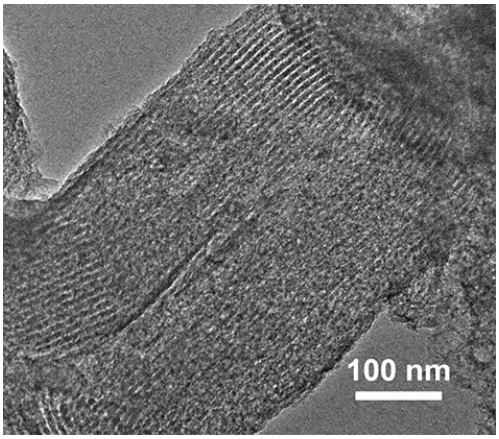

Fig. S2. TEM image of NC.

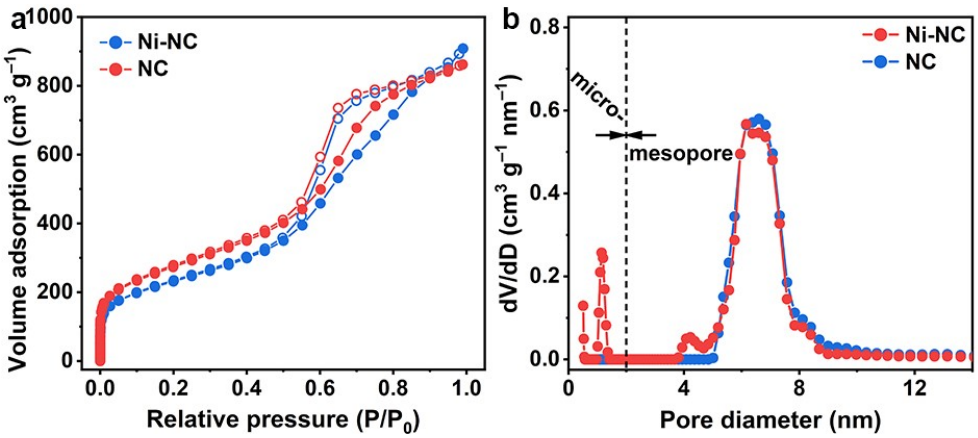

Fig. S3. a) N_2 adsorption-desorption isotherm curves, and b) corresponding pore size distribution of Ni-NC and NC.

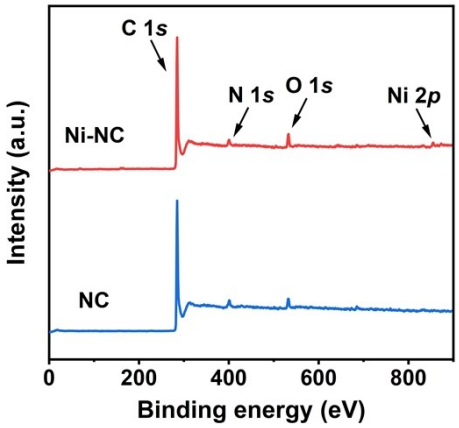

Fig. S4. Comparison referring to the XPS survey spectra of Ni-NC and NC.

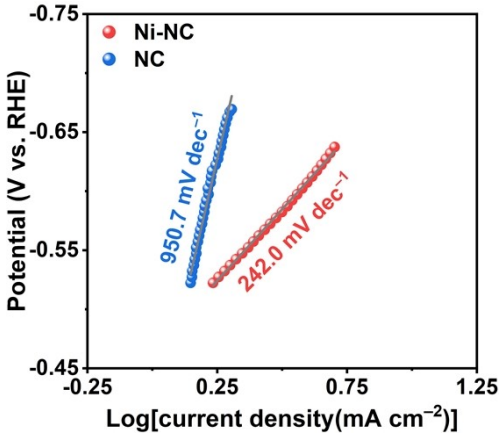

Fig. S5. Tafel slope of Ni-NC and NC under CO_2-saturated condition in 0.5 M $KHCO_3$.

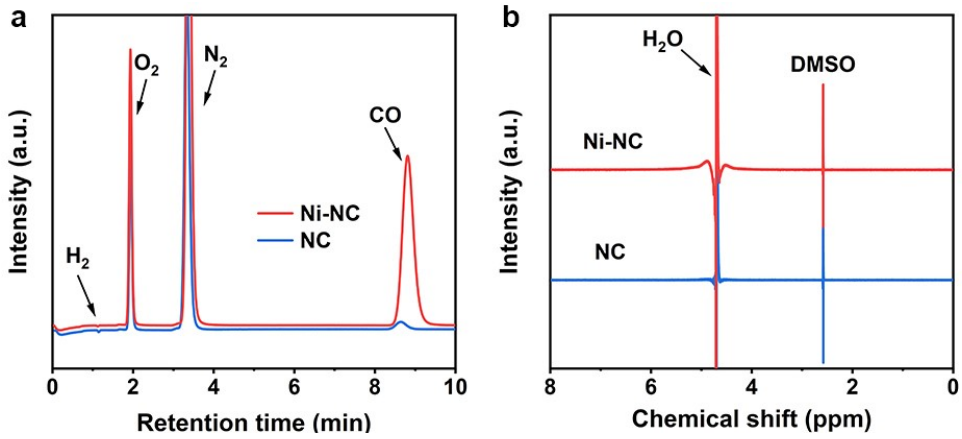

Fig. S6. a) GC's TCD channels of the CO_2RR gas products for Ni-NC and NC at –1.0 V vs. RHE, and b) corresponding ^{1}H NMR spectra of the CO_2RR liquid products for Ni-NC and NC after electrolysis.

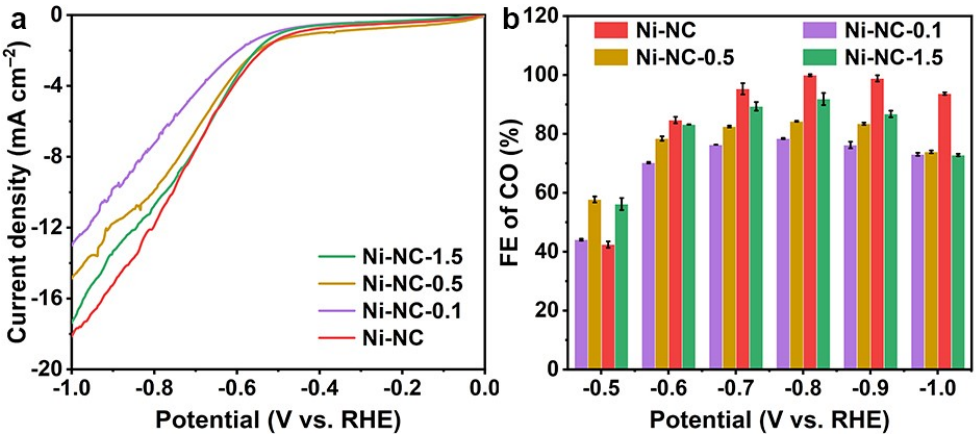

Fig. S7. a) LSV curves and b) FE_{CO} of Ni-NC and Ni-NC-*X* (*X* = 0.1, 0.5, and 1.5) under CO_2-saturated condition in 0.5 M $KHCO_3$.

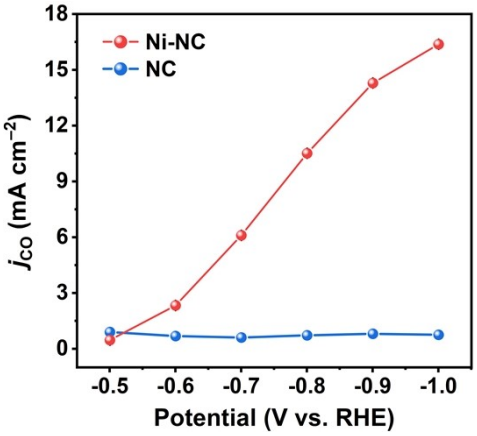

Fig. S8. Calculated j_{CO} of Ni-NC and NC in CO_2RR tests.

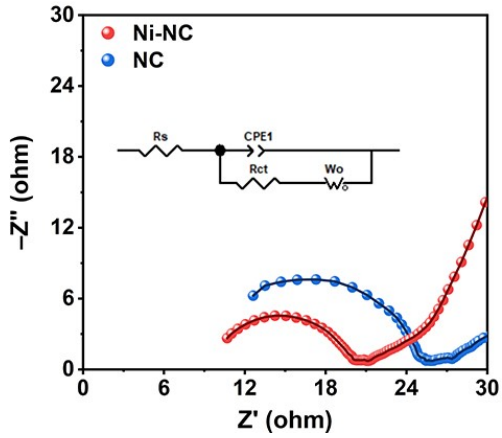

Fig. S9. EIS analysis of Ni-NC and NC in CO_2RR tests.

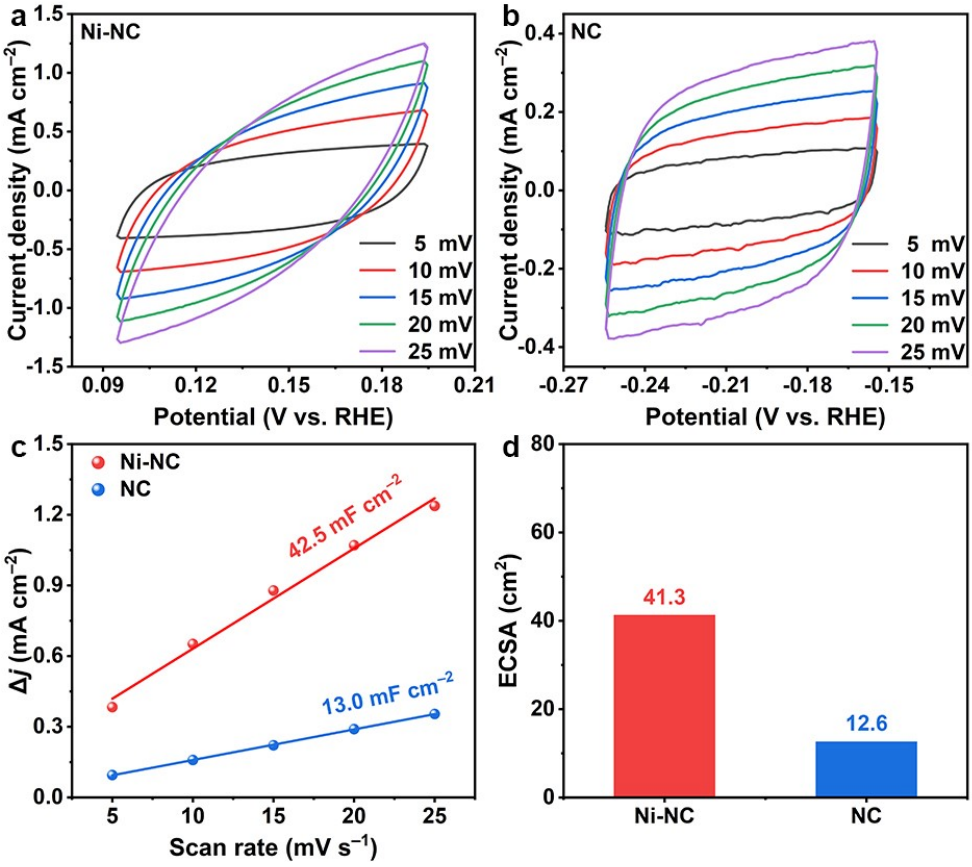

Fig. S10. CVs of a) Ni-NC and b) NC measured in non-Faradaic regions at scan rates of 5 – 25 mV s^{-1} in CO_2RR tests, and corresponding c) C_{dl} and d) ECSA of Ni-NC and NC.

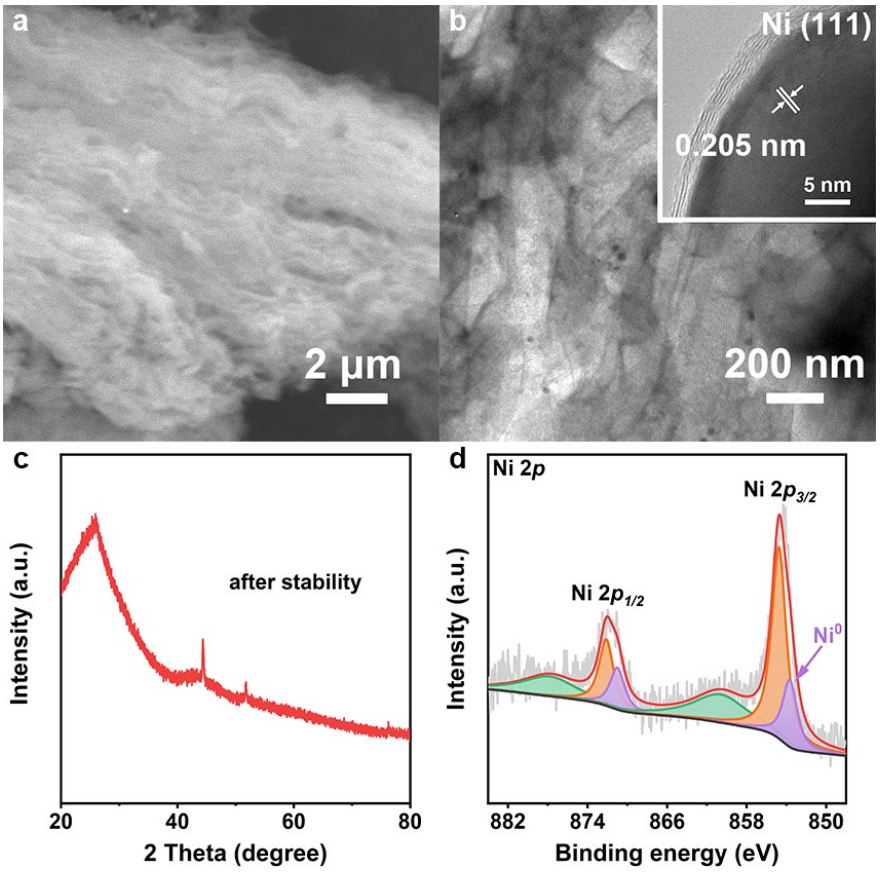

Fig. S11. a) SEM, b) TEM, c) XRD, and d) XPS of Ni 2*p* for Ni-NC after CO_2RR stability test. Inset in b): locally magnified TEM images of Ni NCs.

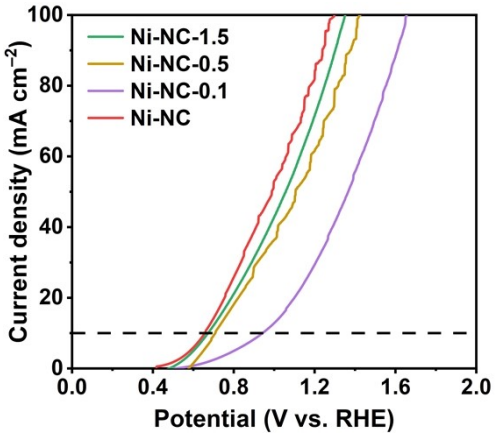

Fig. S12. LSV curves of Ni-NC and Ni-NC-*X* (*X* = 0.1, 0.5, and 1.5) in 1 M KOH with 0.5 M N_2H_4.

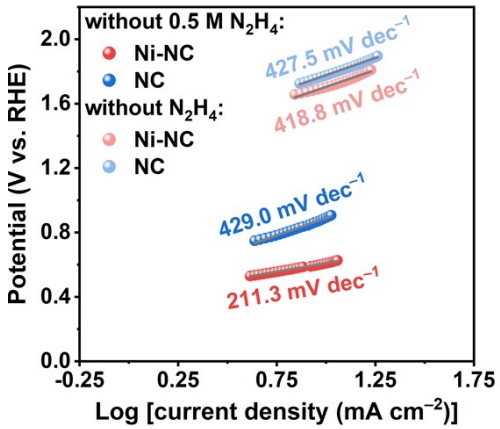

Fig. S13. Tafel slope of Ni-NC and NC in 1 M KOH with and without 0.5 M N_2H_4.

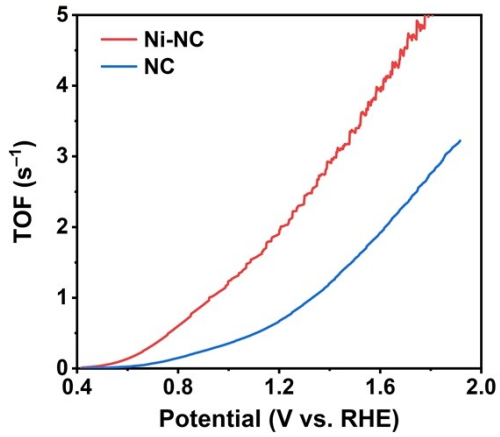

Fig. S14. TOF curves of Ni-NC and NC were derived from the LSV curves.

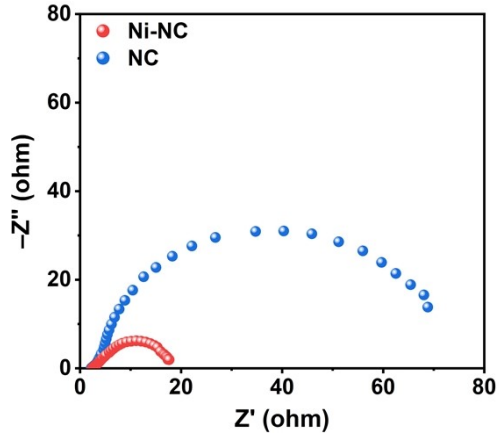

Fig. S15. EIS analysis of Ni-NC and NC in HzOR tests.

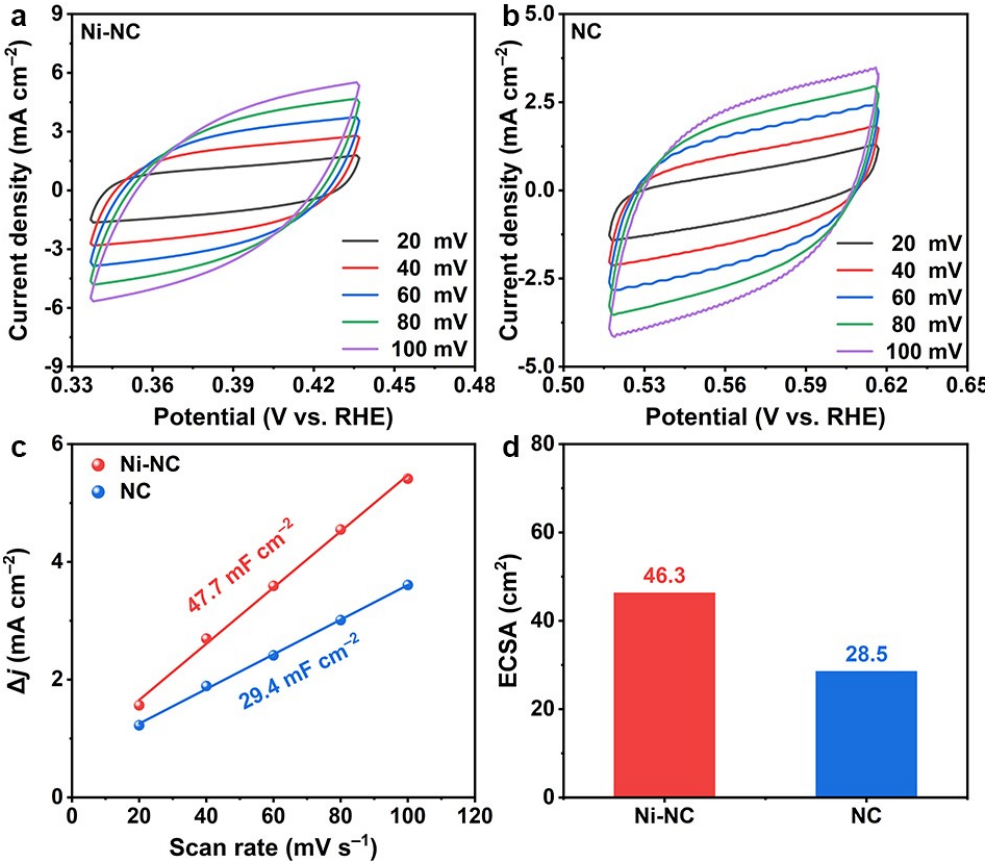

Fig. S16. CVs of a) Ni-NC and b) NC measured in non-Faradaic regions at scan rates of 20 – 100 mV s^{-1} in HzOR tests, and corresponding c) C_{dl} and d) ECSA of Ni-NC and NC.

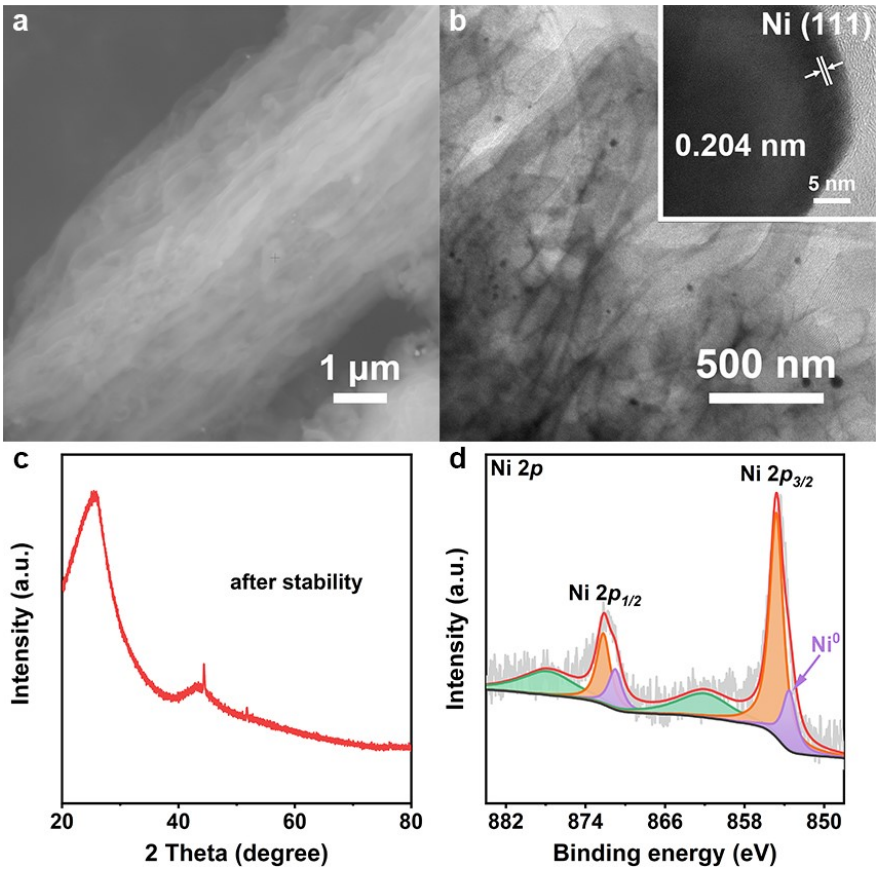

Fig. S17. a) SEM, b) TEM, c) XRD, and d) XPS of Ni 2*p* for Ni-NC after HzOR stability test. Inset in b): locally magnified TEM images of Ni NCs.

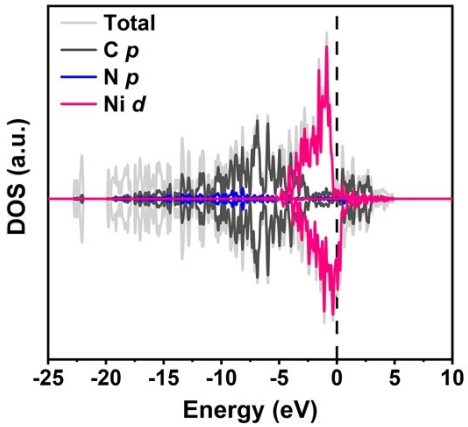

Fig. S18. Density of states for Ni-NC.

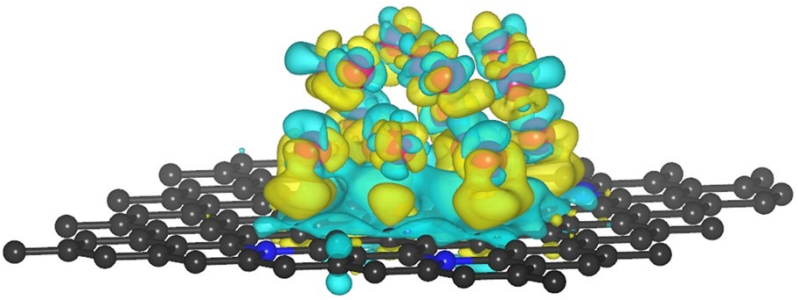

Fig. S19. Differential charge density of Ni-NC (the cyan and yellow areas represent charge consumption and accumulation).

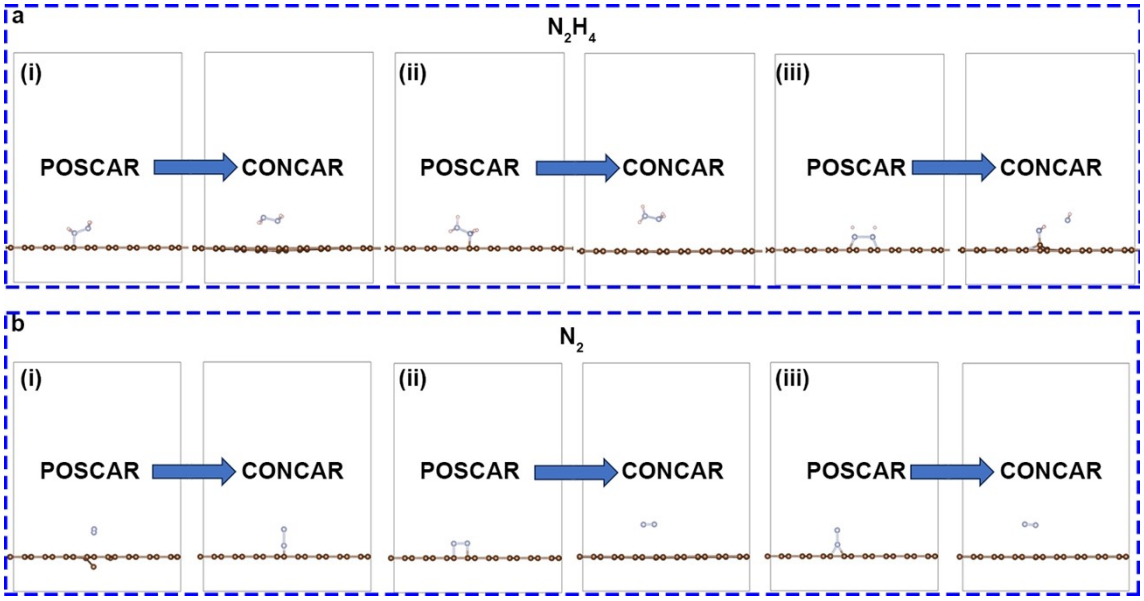

Fig. S20. A comparison of the pre- and post-optimization of several NC adsorption models for a) N_2H_4 and b) N_2.

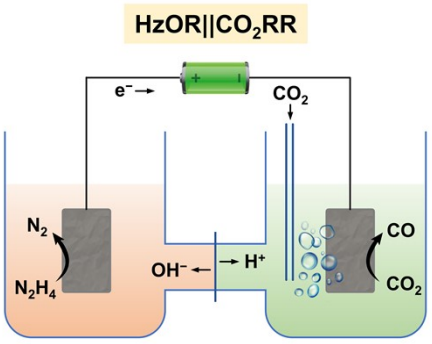

Fig. S21. Schematic illustration of HzOR||CO_2RR in a H-type cell.

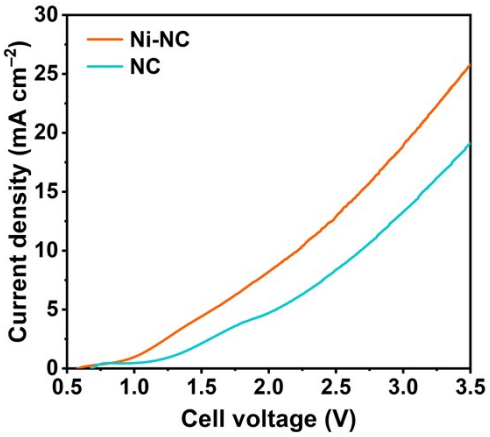

Fig. S22. Polarization curves of Ni-NC-based and NC-based HzOR||CO_2RR.

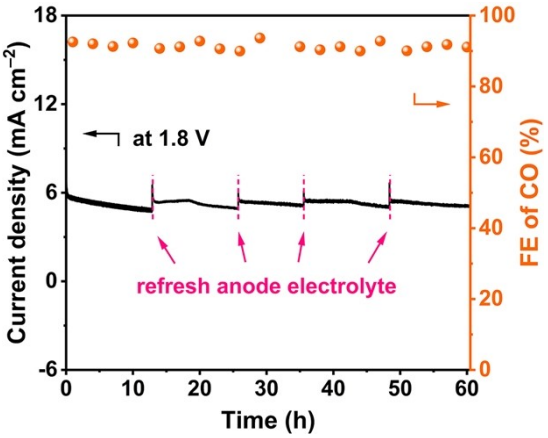

Fig. S23. Stability of Ni-NC for HzOR||CO_2RR in the H-type cell at 1.8 V cell voltage.

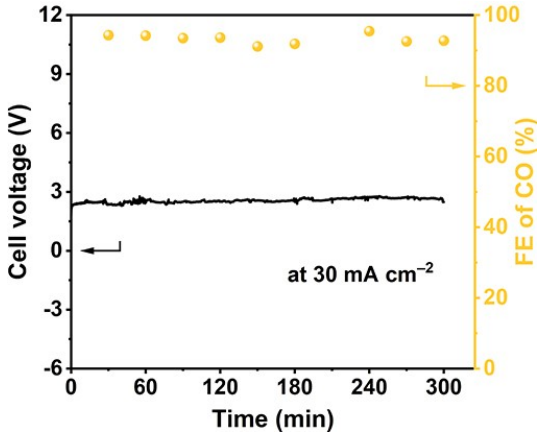

Fig. S24. Stability of Ni-NC for HzOR||CO_2RR in the MEA at 30 mA cm^{-2}.

Table S1. Comparison of specific surface areas and average pore sizes of Ni-NC and NC.

Sample	BET surface area ($m^2\ g^{-1}$)	DFT pore width (nm)
Ni-NC	827.3	6.2
NC	816.5	6.6

Table S2. Comparison of the reported catalysts with the Ni-NC for CO_2 electroreduction to CO in H-type cell.

Sample	Electrolyte	Potential [a] (V vs. RHE)	FE of CO [b] (%)	j_{CO} [c] (%)	Ref.
Ni-NC	**0.5 M $KHCO_3$**	**−1.0**	**94**	**16.4**	**This work**
FeN_4/C	0.1 M $KHCO_3$	−0.6	97	6.87	6
HIE/Ni-N-C	0.5 M $KHCO_3$	−1.0	97	13	7
Ni/NC_PAN_950	0.1 M $KHCO_3$	−0.9	96.5	4.3	8
NiO/Ni-N-C-800	0.1 M $KHCO_3$	−1.0	92	10	9
NC-CNTs (Ni)	0.1 M $KHCO_3$	−1.0	90	10	10
Ni-N-C	0.1 M $KHCO_3$	−1.0	85	17	11
Ni-N_X-C_2	0.1 M $KHCO_3$	−0.7	85	9.5	12
Ni-N-Gr	0.1 M $KHCO_3$	−1.0	85	3.3	13
ACP/S-N-Ni	0.5 M $KHCO_3$	−0.77	80	3.4	14
CNS-NiSA	0.5 M $KHCO_3$	−1.0	74	11	15
Ni-N-C	0.1 M $KHCO_3$	−0.8	69	1	16
Ni-NG	0.5 M $KHCO_3$	−1.0	60	9	17

[a-c] Data were directly obtained from the literature or calculated from the given data.

References

1 C. Hu, Y. Zhang, A. Hu, Y. Wang, X. Wei, K. Shen, L. Chen and Y. Li, *Adv. Mater.*, 2023, **35**, 2209298.

2 X. Zhang, W. Shen, Z. Li, D. Wang, J. Qi and C. Liang, *Carbon*, 2020, **167**, 548−558.

3 X. Liu, J. He, S. Zhao, Y. Liu, Z. Zhao, J. Luo, G. Hu, X. Sun and Y. Ding, *Nat. Commun.*, 2018, **9**, 4365.

4 C. Tang, R. Zhang, W. Lu, Z. Wang, D. Liu, S. Hao, G. Du, A. M. Asiri and X. Sun, *Angew. Chem. Int. Ed.*, 2017, **56**, 842−846.

5 D. Merki, S. Fierro, H. Vrubel and X. Hu, *Chem. Sci.*, 2011, **2**, 1262−1267.

6 C. Liu, Y. Wu, K. Sun, J. Fang, A. Huang, Y. Pan, W. Cheong, Z. Zhuang, Z. Zhuang, Q. Yuan, H. L. Xin, C. Zhang, J. Zhang, H. Xiao, C. Chen and Y. Li, *Chem*, 2021, **7**, 1297−1307.

7 Y. Kong, A. Zheng, Z. Wu, Q. Chen and X. Hu, *Mater. Today Chem.*, 2023, **28**, 101386.

8 M. Zhang, T. Wu, S. Hong, Q. Fan, Y. Soo, J. Masa, J. Qiu and Z. Sun, *ACS Sustain. Chem. Eng.*, 2019, **7**, 15030−15035.

9 H. Li, K. Gan, R. Li, H. Huang, J. Niu, Z. Chen, J. Zhou, Y. Yu, J. Qiu and X. He, *Adv. Funct. Mater.*, 2022, **33**, 2208622.

10 Q. Fan, P. Hou, C. Choi, T. Wu, S. Hong, F. Li, Y. Soo, P. Kang, Y. Jung and Z. Sun, *Adv. Energy Mater.*, 2019, **10**, 1903068.

11 F. Pan, H. Zhang, Z. Liu, D. Cullen, K. Liu, K. More, G. Wu, G. Wang and Y. Li, *J. Mater. Chem. A*, 2019, **7**, 26231−26237.

12 W. Ju, A. Bagger, G. P. Hao, A. S. Varela, I. Sinev, V. Bon, B. Roldan Cuenya, S.

Kaskel, J. Rossmeisl and P. Strasser, *Nat. Commun.*, 2017, **8**, 944.

13 P. Su, K. Iwase, S. Nakanishi, K. Hashimoto and K. Kamiya, *Small*, 2016, **12**, 6083−6089.

14 S. Li, M. Ceccato, X. Lu, S. Frank, N. Lock, A. Roldan, X. Hu, T. Skrydstrup and K. Daasbjerg, *J. Mater. Chem. A*, 2021, **9**, 1583−1592.

15 X. Zhao, S. Huang, Z. Chen, C. Lu, S. Han, C. Ke, J. Zhu, J. Zhang, D. Tranca and X. Zhuang, *Carbon*, 2021, **178**, 488−496.

16 B. J. Park, Y. Wang, Y. Lee, K. J. Noh, A. Cho, M. G. Jang, R. Huang, K. S. Lee and J. W. Han, *Small*, 2021, **17**, e2103705.

17 K. Jiang, S. Siahrostami, T. Zheng, Y. Hu, S. Hwang, E. Stavitski, Y. Peng, J. Dynes, M. Gangisetty, D. Su, K. Attenkofer and H. Wang, *Energy Environ. Sci.*, 2018, **11**, 893−903.